RESEARCH

A biophysically comprehensive model of urothelial afferent neurons: implications for sensory signalling in urinary bladder

Satchithananthi Aruljothi[1] · Rohit Manchanda[1]

Abstract
The urothelium is the innermost layer of the bladder wall; it plays a pivotal role in bladder sensory transduction by responding to chemical and mechanical stimuli. The urothelium also acts as a physical barrier between urine and the outer layers of the bladder wall. There is intricate sensory communication between the layers of the bladder wall and the neurons that supply the bladder, which eventually translates into the regulation of mechanical activity. In response to natural stimuli, urothelial cells release substances such as ATP, nitric oxide (NO), substance P, acetylcholine (ACh), and adenosine. These act on adjacent urothelial cells, myofibroblasts, and urothelial afferent neurons (UAN), controlling the contractile activity of the bladder. There is rising evidence on the importance of urothelial sensory signalling, yet a comprehensive understanding of the functioning of the urothelium-afferent neurons and the factors that govern it remains elusive to date. Until now, the biophysical studies done on UAN have been unable to provide adequate information on the ion channel composition of the neuron, which is paramount to understanding the electrical functioning of the UAN and, by extension, afferent signalling. To this end, we have attempted to model UAN to decipher the ionic mechanisms underlying the excitability of the UAN. In contrast to previous models, our model was built and validated using morphological and biophysical properties consistent with experimental findings for the UAN. The model included all the channels thus far known to be expressed in UAN, including; voltage-gated sodium and potassium channels, N, L, T, P/Q, R-type calcium channels, large-conductance calcium-dependent potassium (BK) channels, small conductance calcium-dependent (SK) channels, Hyperpolarisation activated cation (HCN) channels, transient receptor potential melastatin (TRPM8), transient receptor potential vanilloid (TRPV1) channel, calcium-activated chloride(CaCC) channels, and internal calcium dynamics. Our UAN model a) was constrained as far as possible by experimental data from the literature for the channels and the spiking activity, b) was validated by reproducing the experimental responses to current-clamp and voltage-clamp protocols c) was used as a base for modelling the non-urothelial afferent neurons (NUAN). Using our models, we also gained insights into the variations in ion channels between UAN and NUAN neurons.

Keywords UAN · NUAN · Sensory signalling · Biophysical model · Conductances · Cellular biophysical differences · Urothelial dysfunction · Interstitial cystitis · Sensory signal transduction pathway model · Computational model

✉ Rohit Manchanda
rmanch@iitb.ac.in

Satchithananthi Aruljothi
sachjoe33@gmail.com

[1] Department of Biosciences and Bioengineering, Indian Institute of Technology Bombay, Mumbai 400076, Maharashtra, India

1 Introduction

The urinary bladder is an organ designed for storing and voiding urine. Its functioning is under the elaborate control of neural circuits in the brain, spinal cord, and peripheral autonomic ganglia. The lower urinary tract receives efferent innervation from the thoracic and lumbosacral segments of the spinal cord. Three sets of peripheral nerves carry the efferent signals: sacral parasympathetic (pelvic nerves), thoracolumbar sympathetic (hypogastric nerve), and sacral somatic (pudendal nerves) (Yoshimura & Chancellor, 2003). The afferent axons that innervate the Lower Urinary

Tract (LUT) run in the pelvic, hypogastric, and pudendal nerves, transmitting information to the lumbosacral region of the spinal cord (Andersson, 2002). The pelvic afferent nerves are broadly categorized into myelinated A-delta and unmyelinated C-fibers; they respond to chemical and mechanical stimuli (Groat & Yoshimura, 2009). It is believed that sensitization of these afferents causes bladder hypersensitivity linked to various pathological conditions such as overactive bladder, interstitial cystitis, and painful bladder syndrome (Nickel et al., 2012). The A-delta fibers have larger diameters and transmit action potentials more rapidly than C fibers. Based on their mechanosensitive properties, the pelvic nerves in mice have been classified into four types: muscular, urothelial, muscular/mucosal, and serosal based on stretch, stroke, and probe methods in mice (Groat et al., 2015).

During the filling phase of the bladder, the hydrostatic pressure rises, which increases the activity of the A-delta fibers in the hypogastric and pelvic nerves. The C-fibers respond to nociceptive stimuli such as chemicals, inflammation, and elevated intravesical pressure. During normal bladder filling, the C-fibers are quiescent, and their activation may indicate pathological disorders of the bladder (Merrill et al., 2016). The urothelium modulates the afferent nerve activity by releasing mediators which act upon the afferent nerve terminals (Apodaca et al., 2003). The proximity between afferent neurons and the urothelium implies that any abnormal sensations in the urothelium can lead to aberrant sensory signals transmitted through afferent nerves. Conditions such as Overactive Bladder (OAB) syndrome, characterized by heightened spontaneous contractions of the bladder wall, may involve the release of chemical agents from the urothelium (Andersson & Arner, 2004). Understanding the origins of this spontaneous activity is crucial for effectively treating OAB. Furthermore, there is mounting evidence indicating that the urothelium possesses sensory properties essential for detecting and relaying both physiological and noxious signals (Birder & Groat, 2007). This sensory function is facilitated by the presence of receptors, neurotransmitters, and neurons within the urothelium. Notably, bladder afferent and efferent nerve terminals are closely situated to the urothelium, with some axon terminals even residing within it (Birder & Groat, 2007). These neurons are called the urothelial afferent neurons (UAN). The C-fiber afferent bladder neurons innervating other parts of the bladder are termed the non-urothelial afferent neurons (NUAN) (Kanda et al., 2016). Kanda et al. (2016) showed that the UAN and NUAN neurons differed in their morphological and biophysical properties such as rheobase, input resistance, membrane capacitance, the amplitude of inactivating and sustained K+ currents and rebound action potential firing (Kanda et al., 2016). These new insights led to further open questions concerning the UAN and NUAN, such as

the underlying ion channel composition in these neuronal cell-types and the variations that give rise to such differences. Addressing the underlying ion channel composition in both urothelial afferent neurons (UAN) and non-urothelial afferent neurons (NUAN) holds paramount importance in advancing our understanding of sensory signalling in the urinary bladder. This knowledge forms the bedrock for unraveling the intricate biophysical mechanisms governing the behavior of these neurons. Moreover, it sheds light on why UAN and NUAN neurons exhibit distinct sensitivities and responses to stimuli, paving the way for a more comprehensive classification of bladder afferent neurons. Beyond fundamental research, discerning the specific ion channels present in these neurons has direct clinical implications. It provides potential targets for pharmacological interventions, potentially revolutionizing the treatment landscape for bladder-related disorders. This knowledge also offers the groundwork for personalized medicine, enabling tailored interventions based on the individual ion channel expression profiles. Furthermore, it guides the development and screening of pharmaceutical agents, particularly those modulating sensory signalling in the urinary bladder. Ultimately, this foundational understanding serves as a launchpad for in-depth investigations into the molecular mechanisms and interactions that underlie sensory signalling in the urinary bladder, propelling the field towards more effective therapeutic strategies. Our study aims to validate and refine these observations through computational modeling, with a focus on the contributions of specific ion channels, such as Kv1.4, Kv4, T-type Ca2+, and HCN channels, in shaping the excitability profiles of UAN and NUAN.

It is difficult to address such questions experimentally for the following reasons a) technical challenges associated with performing patch-clamp recordings in intact Dorsal Root Ganglion (DRG) soma preparation. b)the UAN and NUAN express a wide range of ion channels, and the interactions between the different ionic currents and their modulation govern the regular and pathological activity of the LUT; this further adds to the complexity of performing experimental studies. In such a scenario, a computational model is highly useful in performing various analyses.

A computational model could also help elucidate these variations to understand the ionic mechanism behind the greater excitability of UAN compared to NUAN. It is also an alternative to wet lab work to predict the possible variations in the membrane properties that can mimic UAN and NUAN satisfactorily. There are pre-existing computational models of non-specific large diameter myelinated DRG neurons with the transient Hodgkin-Huxley type voltage-dependent INa^+ and ohmic leak modeled by Amir and Devor (2003a, b). A similar large diameter DRG neuron with HH-type currents, fast active tetrodotoxin-sensitive Na^+ current, and a passive outward IK^+ current was modelled by Kovalsky

(2009). Sundt et al. (2015) reported a model of unmyelinated DRG C-fiber consisting of the following channels: NaV, KCNQ (KV7), L-type Ca, and SK (Sundt et al., 2015). All of the models mentioned above of the DRG neurons are either non-specific or large-diameter neurons. A more recent biophysically constrained model of the bladder DRG C-fiber was developed by Mandge and Manchanda (2018) with 22 membrane mechanisms including Na^+, K^+, Ca^{2+}, Cl^-, and some non-specific ion channels such as TRPM8, HCN and passive channels as well as pumps such as Na^+/K^{+-}ATPase Pump, PMCA pump and Na^+/Ca^{2+} exchanger (NCX) along with an elaborate calcium dynamics (Mandge & Manchanda, 2018).

Since we are modelling a bladder UAN, the C-fiber DRG soma model by Mandge and Manchanda (2018) was the closest biophysically; hence we tried to adapt this model for the UAN and found that the model could not be used in its current form. The model needed morphological and biophysical modifications and additions in order to be used as a UAN model. Morphologically the Mandge and Manchanda (2018) model had only a soma. Still, the UAN model would require an additional stem and central and peripheral branches as the experiments done on UAN were on intact neurons with the soma, stem, and branches (Kanda et al., 2016). Biophysical modifications were required for the DRG model (as described in the later sections) since the DRG model failed to replicate the traces for the UAN total current recordings. Hence, we have exclusively modelled a biophysically realistic model of the UAN with stem, central, and peripheral axon branches in addition to the soma as per the experimental setup by

using the parameters for the UAN (see Fig. 1). The model was validated against experimental data for action potential, total membrane current, and rebound APs.

We have used a validated model to test experimental predictions, verify hypotheses, and shed new insights into the functioning of the UAN. In our investigation, we focused on determining the specific potassium (Kv) channel types responsible for the observed A-type currents. This question holds substantial importance as A-type K^+ currents play a pivotal role in regulating sensory neuron excitability (Takahashi et al., 2013). Our simulations, incorporating various Kv channel candidates, revealed a compelling insight. Among the three potential candidates, Kv1.4, Kv1.1, and Kv4, our model provided robust evidence supporting the significant presence of Kv1.4 and Kv4 channels in the UAN. This finding not only sheds light on the biophysical distinctions between UAN and NUAN but also addresses a vital query posed by experimentalists (Kanda et al., 2016). Given its relevance to the understanding of sensory signalling mechanisms, we emphasize the pivotal role of Kv1.4 and Kv4 channels in modulating UAN excitability. This discovery serves as a cornerstone for future studies exploring the intricate interplay between ion channels and their functional implications in urothelial afferent neurons. By elucidating the specific Kv channel composition, our work provides a key building block towards a comprehensive understanding of sensory signalling in the urinary bladder. One of the striking outcomes of the Kanda et al. (2016) experiment was to indicate the difference in UAN and NUAN neurons with the presence and absence of the rebound action potential in UAN and NUAN, respectively,

Fig. 1 Computational morphology of UAN and NUAN neuron

(a) Urothelial

(b) Non-urothelial
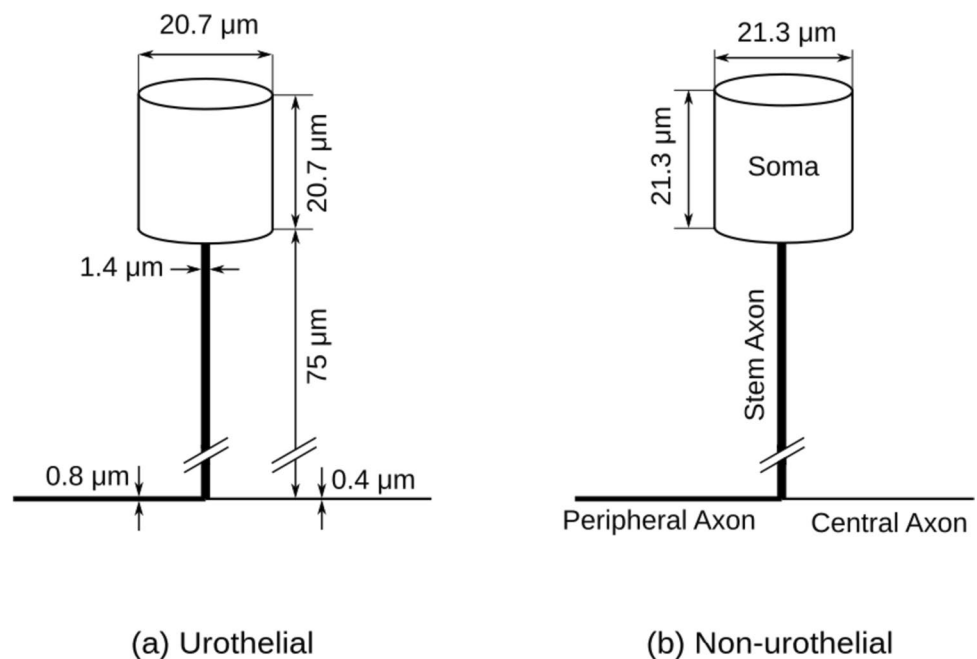
following prolonged hyperpolarisation. We tested our model to see if we could replicate this phenomenon. We used a hyperpolarsing current pulse similar to the one used experimentally and obtained a rebound AP in the UAN while failing to obtain it in the NUAN. Our model suggests that the presence of a larger conductance density of HCN and CaT in UAN compared to the NUAN was the reason behind the presence and absence of rebound AP in the UAN and NUAN. We have rigorously validated our model against experimental current and voltage traces.

In the work presented here, besides modelling a urothelial and a non-urothelial afferent neuron, we accounted for the difference in their biophysical properties previously unexplained by experiments.

2 Methods

2.1 Computational model

We used the NEURON simulation environment (Hines & Carnevale, 1997) to construct the UAN model and perform our simulations. The UAN is a pseudo-unipolar neuron; hence we constructed the morphology of the UAN model comprising a soma, a stem, a central branch, and a peripheral branch (see Fig. 1). We used a similar approach as the bladder DRG soma modelled by Mandge and Manchanda (2018), with the morphological and biophysical parameters modified to fit the UAN model. The biophysical parameters for the model were tuned to fit the properties of UAN neurons observed in vitro. The experimental data specific to the UAN model were obtained from Kanda et al. (2016), and the additional data not present in Kanda et al. (2016) were obtained from Du et al. (2014). We digitised the experimental plots for comparison with the simulated results using Webplot Digitiser (Rastogi et al., 2008), an online tool to extract numerical data from plots.

Code accessibility The source code for the proposed UAN model is available on the GitHub server https://github.com/sachjoe/BiophysicalmodelUAN.git.

2.2 Morphological parameters in the model

Patch clamp recordings from neurons in the dorsal root ganglia (DRGs) have vastly expanded our knowledge of the functioning of these neurons. The bulk of recordings are currently done on dissociated DRG neurons, which is a standard preparation in most investigations. However, axonal damage caused by enzyme digestion used to obtain dissociated neurons might affect neuronal characteristics. Furthermore, detached neuron preparations do not accurately replicate the DRG's microenvironment. Most studies done on bladder

DRG (Hayashi et al., 2009), Yoshimura and Yamaguchi (1997) are from acutely dissociated DRG neurons; hence the Mandge and Manchanda (2018) model consisted of only the soma. In order to overcome the limitations of the conventional dissociated DRG neurons for patch clamp recordings, Newer studies were conducted in intact DRG (Kanda et al., 2016), where both the peripheral and central branches of the neurons were preserved. This enabled us to model the pseudo-unipolar urothelial bladder neuron as a whole, with the soma, stem, and branches. This helps simulate the electrophysiological behavior of the UAN more accurately and renders it physiologically more realistic.

The morphological parameters used in UAN and NUAN models were taken from the literature (Kanda et al., 2016; Du et al., 2014). The UAN and NUAN are modelled as cylindrical somata of diameter 20.7 μm, and 21.3 μm (Kanda et al., 2016), respectively. In both cases, the soma is attached to an unmyelinated initial short stem axon of diameter 1.4 μm and length 75 μm (Du et al., 2014), which bifurcates into a peripheral branch of diameter 0.8 μm (Du et al., 2014) and length 100μm and a central branch of diameter 0.4 μm (Du et al., 2014) and length 100μm. We have illustrated the computational models in Fig. 1. In all the simulations, we have kept axonal length and diameter constant. We have listed in Table 1 all the parameters used in the model. As seen from Table 1, the diameter of the UAN is approximately a micrometre smaller than the NUAN. The dimensions of the stem, peripheral, and central branches were kept similar for both axons (Du et al., 2014).

2.3 Biophysical parameters in the UAN and NUAN models

Passive and active properties were added to both UAN and NUAN models. The specific membrane resistance (R_m) of 10000 Ωcm^2) (Choi & Waxman, 2011) was kept constant for all sections in both UAN and NUAN. Experimental studies reported the total membrane capacitance as 18.0 $\pm$ 1.6 pF for UAN, and 24.5 $\pm$ 2.5 pF for NUAN (Kanda et al., 2016). These values were used in our model. Passive conductance is ($gpas$) = 1/Rm = 1/(10000 Ωcm^2) = 1$\times$10^{-4} S/cm^2 and kept the passive potential (Epas) at -73 mV to set the Resting Membrane Potential (RMP) at -73 mV (Kanda et al., 2016) for both UAN and NUAN. The RMP was reported to be identical in both neurons (Kanda et al., 2016).

The models include 25 different voltage-dependent and calcium-dependent ionic channels distributed in the soma, stem, and branches uniformly (Table 2). To achieve satisfactory fits for the UAN and NUAN experimental recordings, the maximum conductance values for each ionic current were tuned.

The general approach to model the properties of different ionic currents in both UAN and NUAN is based on the

Table 1 Morphological and biophysiological parameters used in the model

Parameters	UAN model	NUAN model	Reference
Soma diameter (μm)	20.7	21.3	Kanda et al. (2016)
Stem axon diameter (μm)	1.4	1.4	Du et al. (2014)
Stem axon length (μm)	75	75	Du et al. (2014)
Central axon branch dia (μm)	0.4	0.4	Du et al. (2014)
Peripheral axon branch dia (μm)	0.8	0.8	Du et al. (2014)
RMP (mV)	−73	−73	Kanda et al. (2016)
Total membrane capacitance (pF)	18	24.5	Kanda et al. (2016)
Input resistance (Mω)	474.2	332.1	Kanda et al. (2016)
Rebound action potential	Yes	No	Kanda et al. (2016)
Rheobase (pA)	100.3	301	Kanda et al. (2016)
Temperature °C	22	22	Kanda et al. (2016)

Hodgkin-Huxley-type formalism (Hodgkin & Rushton, 1946). The time integral equation used to calculate the transmembrane voltage is given by;

$$\frac{dV}{dt} = -\frac{1}{C_m} \times \left\{ \sum [g_w \times (V - V_w)] + i_{stim} \right\}$$

where V is the membrane potential, C_m membrane capacitance, w denotes the wth channel type, g_w ionic conductances of various channels present in the model, and V_w is the reversal potentials (the subscript w denotes different channels), and i_{stim} is the stimulus current injected. Membrane conductances of the ion channels were represented as

Table 2 Ion channels present in Mandge and Manchanda (2018) (DRG) model and the UAN model

Ion channels	DRG / NUAN model	Reference
Tetrodotoxin-Sensitive (TTX-S)	DRG,UAN	Baker (2005)
Tetrodotoxin-Sensitive (TTX-R)	DRG	Yoshimura (1999)
Nav1.7	UAN	Chambers et al. (2014)
Nav1.8	DRG,UAN	Han et al. (2015)
Nav1.9	DRG,UAN	Black et al. (2003)
A-type K$^+$ (KA)	DRG	Black et al. (2003)
Kv1.4	UAN	Black et al. (2003)
Kv1.1	UAN	Akemann et al. (2009)
Kv4	UAN	Black et al. (2003)
Kv4.3	UAN	DeBerry et al. (2013)
Delayed Rectifier (KDR)	DRG,UAN	Yoshimura et al. (2006)
Large-Conductance Ca^{2+}-Activated K$^+$ (BKCa)	DRG,UAN	Shieh et al. (2007)
Small-Conductance Ca^{2+}-Activated K$^+$ (SKCa): hSK3	DRG,UAN	Hougaard et al. (2009)
KCNQ/M	DRG,UAN	Passmore et al. (2003)
Na+-activated K+ (KNa)	DRG,UAN	Bischoff et al. (1998)
L-type Ca^{2+}	DRG,UAN	Tong et al. (2011)
N-type Ca^{2+}	DRG,UAN	Tong et al. (2011)
P/Q-type Ca^{2+}	DRG,UAN	Fukumoto et al. (2012)
R-type Ca^{2+}	DRG,UAN	Hilaire et al. (1997)
T-type Ca^{2+}	DRG,UAN	Fox et al. (1987)
Hyperpolarization-Activated Cyclic Nucleotide-Gated	DRG,UAN	Matsuyoshi et al. (2006)
Store-Operated Ca^{2+} (SOCC)	DRG,UAN	Usachev and Thayer (1999)
Ca^{2+}-activated Cl$^-$ (CaCC)	DRG,UAN	Salzer et al. (2016)
Transient Receptor Potential Melastatin (TRPM8)	DRG,UAN	Hayashi et al. (2009)
Transient Receptor Potential Cation Channel (TRPV1)	UAN	Aruljothi et al. (2017)

$$g_w = G_{max_w} \times x_w^{z_w} \times y_w$$

where G_{max_w} is the maximum ionic conductance, x_w and y_w are the state variables for a gating particle, and z_w is the number of gating particles. The equation that relates x and y to the first order rate constants α and β is

$$x_\infty = \frac{\alpha_x}{\alpha_x + \beta_x}$$

$$y_\infty = \frac{\alpha_y}{\alpha_y + \beta_y}$$

$$\tau_x = \frac{1}{\alpha_x + \beta_x}$$

$$\tau_y = \frac{1}{\alpha_y + \beta_y}$$

The state variable kinetics is given by

$$\frac{dx}{dt} = \frac{x_\infty - x}{\tau_\infty}$$

$$\frac{dy}{dt} = \frac{y_\infty - y}{\tau_\infty}$$

α and β are functions of voltage. We have shown in Table 3 the parameterized equations for the α and β for the ionic current that were not present in the Mandge and Manchanda (2018) model.

2.4 Simulation protocol used in UAN and NUAN model

In all models, we performed the stimulations and recording at the soma. To determine the voltage-activated currents, we performed a voltage-clamp simulation in voltage steps for clamp potentials ranging from –90 to +70 mV in 10 mV increments and of duration 250 ms.

We used step current pulses of amplitude ranging between –120 and +120 pA (20 pA per step, 1000 ms duration) to evoke action potentials and determine membrane excitability. According to the experimental studies, we kept the simulation protocols the same for all the models.

2.5 The three-phase model used for the selection of ion channels in the UAN

Methodology The first step towards modelling the UAN was to test if the available pre-existing models could be used as a UAN model. In order to do that, We examined the soma model of the neuron presented in Mandge and Manchanda (2018). We endowed it with the morphological parameters and passive membrane properties of the UAN as obtained from the experimental studies (Kanda et al., 2016). We kept the ion channel mechanisms unchanged since there was no information on the types of the ion channels in the study. Next, we tested our model against UAN experimental recordings. Using voltage steps of 10 mV from –60 mV for a duration of 250 ms, we employed the voltage clamp simulation procedure to model the total membrane current in accordance with the experimental investigations and

Table 3 Voltage-dependent conductance parameters. The variables used in expressions for α and β are v membrane depolarization in mV, v_s shift voltage in mV, and T absolute temperature in K

Conductance State variables		n	G_{max} (mS/cm^2)	V_{rev}(mV)	α (s^{-1})	β (s^{-1})	[Ref]
$g_{Nav1.7}$	Activation	3	2.3	50	$0.42 \times (v+35)/(1 - e^{\frac{-(v+35)}{10}})$	$16.7 \times e^{-0.055(v+60)}$	[1], [2]
	Inactivation	1			$0.29 \times e^{-0.3(v+60)}$	$4.17/(1 + e^{\frac{-(v+27)}{5}})$	
$g_{Kv1.1}$	Activation	4	0.096	−77	$0.13 \times e^{\frac{-(v+45)}{-33.9}}$	$0.13 \times e^{\frac{-(v+45)}{12.4}}$	[3]
$g_{Kv1.4}$	Activation	4	2.15	−77	$0.01 \times (-55 + v_s - v)$	$0.125 \times e^{\frac{-65+v_s-v}{80}}$	[4]
	Inactivation	1			$25.6 \times 10^{-6} \times e^{\frac{v_s-v}{45.4}}$	$0.033/(1 + e^{\frac{-45.67+v_s-v}{2.3}})$	
g_{Kv4}	Activation	4	0.002	−77	$0.15743 \times e^{\frac{-(v+57)}{-32.1997}}$	$0.15743 \times e^{\frac{-(v+57)}{37.514}}$	[5]
	Inactivation	1			$0.01342/(1 + e^{\frac{-(v+60)}{-7.864}})$	$0.04477/(1 + e^{\frac{-(v+54)}{11.3615}})$	
$g_{Kv4.3}$	Activation	3	0.00001	−77	$2.4441 \times e^{-23.32\times(v+9.17203)}$	$0.4965 \times e^{-19.47\times(v+18.28)}$	[6]
	Inactivation	1			$0.331 \times e^{-12.8433\times(v+111.332)}$	$0.3105 \times e^{-8.9\times(v+49.95)}$	
g_{TRPV1}	Activation	1	0.05	0	$1.6 \times 10^{37} \times e^{\frac{-2.08\times10^5+34.26v}{8.314\times T}}$	$9.67 \times 10^5 \times e^{\frac{-2.32\times10^4+34.26v}{8.314\times T}}$	[7]

The references indicated are: [1] Chambers et al. (2014); [2] Akemann et al. (2009); [3] Solinas et al. (2007); [3] Schmidt-Hieber and Bischofberger (2010); [5] Akemann and Knöpfel (2006); [6] Masoli et al. (2015); and [7] Aruljothi et al. (2017)

compare the results to the experimental response. The maximum conductances of the channels were fine-tuned both manually and using an automated method available in the NEURON platform to get the closest fit between simulated and experimental waveforms.

Observation In the total membrane current response from the experimental recording, three distinct phases are observed (see Fig: 2A) as follows; phase 1, a transient inward current at the beginning of the voltage steps, phase 2, an outward current, and phase 3, sustained non-inactivating outward currents. Comparing the total current response of the DRG model with that of the experimental response (see Fig: 2B), a clear difference in all three phases was discerned.

Ion Channel contributions to UAN function The total membrane current response of the UAN exhibits three distinct phases, with phase 1 showing a transient inward current primarily due to the activation of voltage-gated Na^+ channels, phase 2 showing an outward current due to the activation of inactivating and non-inactivating voltage-gated K^+ channels (KA type channels), and phase 3 showing sustained non-inactivating outward currents due to Kdr-type currents. However, the total current response from the DRG model differed significantly from the experimental response in all three phases (see Fig. 2B). This discrepancy indicates that additional Na^+, KA, and possibly Kdr-type channels are required for the UAN.

Identification of additional channels To address the need for additional ion channels, we conducted a comprehensive review of the literature on UAN and identified potential candidate channels based on their biophysical properties. In the following sections, we provide a detailed account of our selection of additional Na^+ and K^+ channels and their contributions to the UAN function.

2.5.1 Selection of sodium ion channels

The predominant sodium channels expressed in DRG afferent neurons are TTX sensitive (TTXs) (Yoshimura, 1999), Nav1.8 (Ritter et al., 2009), Nav1.9 (Ritter et al., 2009), and Nav1.7 (Lei et al., 2013). Equations for Nav currents for phase 1 are adapted from TTXs, Nav1.8 and Nav1.9 from (Mandge & Manchanda, 2018) and Nav1.7 from (Chambers et al., 2014).

2.5.2 Selection of potassium ion channels

We have shown in Fig. 2B that the existing K^+ channels, generic KA, and Kdr in the small DRG soma model were inadequate to match the simulated total current with the experimental one for the UAN. Since the A-type K^+ currents were known to regulate sensory neuron excitability (Takahashi et al., 2013), it was speculated that Kv4.3 or Kv1.4 could be the channels responsible for the A-type current (Kanda et al., 2016).
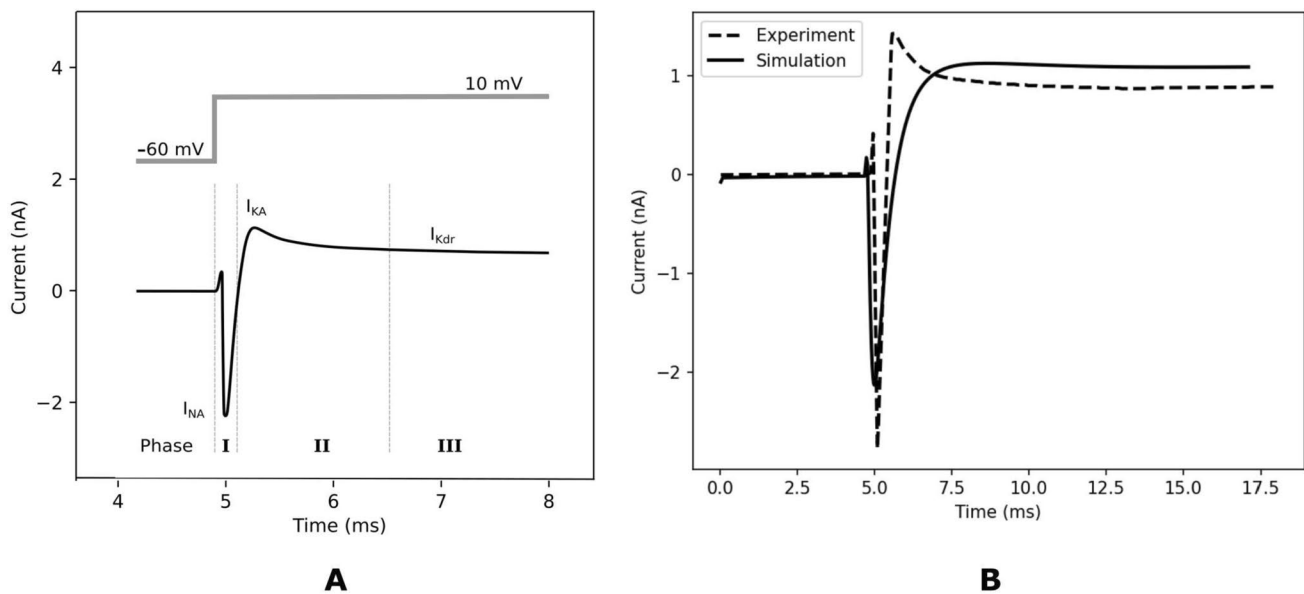

Fig. 2 A: Three phases in the experimental voltage clamp trace stepped from -60 mV to 10 mV adapted from (Kanda et al., 2016). Phase 1 is a transient inward current due to the sodium channels. Phase 2 is the transient outward current due to the KA-type potassium channels. Phase 3 is the sustained non-inactivating outward current due to the Kdr-type channels. **B**: The experimental recording (dashed lines) shows the total membrane current elicited in the UAN by a 250 ms voltage step from -60mV to 10mV (Kanda et al., 2016). The solid lines show the simulation result from the DRG model

For phase 2 Due to the fast inactivation in phase 2 of the experimental curve, we examined A-type potassium channels. We have added the specific KA type channel Kv1.4 Kv4 and Kv4.3, which were known to be present in the bladder (Takahashi et al., 2013).

For phase 3 Since the experimental trace showed a slower activating and non-inactivating outward current, the Kdr channels are most likely to underpin the current. To bridge the difference in the trace in phase 3, we included Kv1.1 and Kdr-type channels present in the DRG model. Studies have shown the presence of Kv1.1 in the bladder afferent neurons (Takahashi et al., 2013). The ion channels present in the UAN and the DRG are tabulated in Table 2.

2.6 Model tuning and testing

In the UAN and NUAN models, after the model construction with the morphological, passive properties and setting of the ionic channel properties, the maximum ionic conductances of voltage- and calcium-dependent channels remained the free parameters. These were pre-determined based on experimental estimations obtained from the literature and were fine-tuned through trial and error. In complex neuron models, a pertinent challenge and time-consuming step is the precise calibration of the multiple ionic channel conductances involved. In addition to using the automated optimization algorithm (multiple run fitter) provided in the NEURON software, we used manual tuning to get a better fit.

We tested the matching of the model output to that of experimental data by comparing their voltage traces elicited in response to the current clamp. We tuned the parameters by altering the maximum conductances.

2.7 Statistical analysis

The experimental data published in the literature were digitized using WebPlotDigitizer (2022) for the analysis. We used the Root Mean Square Error (RMSE) measure for the time-dependent waveform to statistically calculate the match between the experimental data and the DRG, UAN, and NUAN models. The RMSE value is calculated using the corresponding samples between the experimental and simulated data, and the difference between them is evaluated as an RMSE measure. The lesser the RMSE value, the better the match.

$$RMSE = \sqrt{\frac{\sum_N E_i^2}{N}} \tag{1}$$

where i represents the sample number in experimental data. The time instant of each sample in the experimental data was observed, and the corresponding sample point from the

simulated data was chosen for calculating the error E_i for the ith sample. N is the total number of samples. The original formula given in Eq. (1) does not include the time interval between the samples and assumes that the samples are equally spaced. This leaves room for misevaluation of the RMSE value. Therefore, a modified version of the RMSE, as given in Eq. (2) was used for quantifying the similarity between the simulated data and the corresponding experimental trances.

$$RMSE_t = \sqrt{\frac{\sum_{N-1} E_i^2 * dt_i}{T}} \tag{2}$$

where dt_i is the time interval between the ith sample and $(i+1)$th sample, total time duration of the data $T = \sum_{N-1} dt_i$. Equation (1) is a special case of Eq. (2) with $dt_i = 1$ for all i.

2.8 Feature measurement for total membrane current

To evaluate the accuracy of our model, we compared the simulated membrane current with an in-vitro experiment using a voltage clamp set at 10 mV (Kanda et al., 2016). To obtain a quantitative evaluation, we defined a set of features for the recorded current, including peak hyperpolarising (A_1, nA) and depolarising currents (A_2, nA), as measurements for the maximum amplitude of negative and positive currents, fall (t_f, ms) and rise time (t_r, ms), as the time taken to reach 90% peak values, and the exponential fall observed after the peak positive current as decay time constant (τ, ms), and full width at half maximum amplitude – 1 (called half-width-1 or HW_1 for convenience, in ms) and full width at half maximum amplitude – 2 (HW_2, ms) at the negative and positive phases shown in Fig. 3A. For the half-width measurements, we evaluated the width of the negative and positive phases at 50% of peak hyperpolarising current and peak current relative to the saturation current, respectively. The start and endpoints of the measurements were marked in Fig. 3A. The accuracy of our model was determined by comparing the simulated and recorded currents for each feature. These salient features provide a comprehensive evaluation of the accuracy of our model in simulating membrane currents.

2.9 Feature measurement for action potential

In order to compare the closeness of the simulated curve to that of the experimental counterpart, we carried out feature estimation for AP using the following measurements shown in Fig 3B. For the AP, the measurements included the **amplitude (mV)**, **width (full width at half maximum)**, **after-hyperpolarization (AHP)**, **foot width**, and **foot area**. The **amplitude** is the depolarization measured
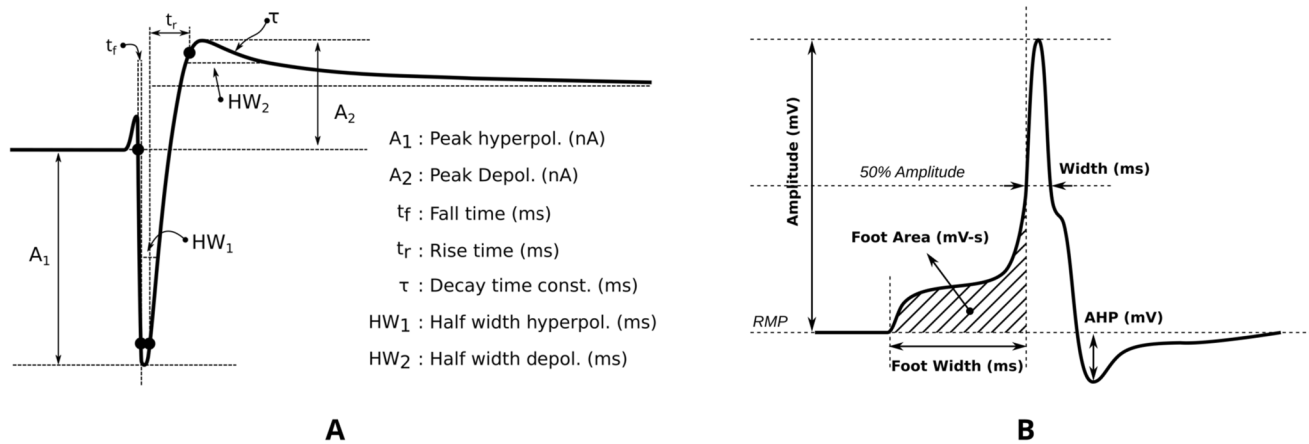
Fig. 3 **A**: Feature measurement of Total membrane current and **B**: Feature measurement of AP, for the comparison between the experimental and simulated outcomes

from the resting potential to the peak of the spike. The **width** is the time period between the AP's ascending and descending phases at 50% of the peak amplitude. **AHP** is the difference in time between the resting membrane potential (RMP) and the first local minimum after the AP peak. The **AP foot**, which is the region between the stimulus and the AP onset, was analyzed with two features: **foot width** and **foot area**. **Foot width** is the duration between the AP onset and the instant when the membrane potential reaches 50% of the peak value. **Foot area** is the area measured between the RMP and the AP foot. The total membrane current was evaluated using salient features, such as the peak hyperpolarizing current, peak depolarizing current, fall time, rise time, decay time constant, half-width 1, and half-width 2. The simulated curves were compared with experimental counterparts to determine the accuracy of the model. The feature measurements allowed for quantitative evaluations and comparisons of the simulated and experimental results.

3 Results

3.1 Urothelial neuron model

In this work, we built a biophysically detailed, physiologically constrained model of the UAN and the NUAN. To assess the robustness of the models, we compared the experimental recordings of the total membrane current (I_{total}) and action potential (AP) with the simulated results. To validate the model, we compared the simulation results with experimental traces of I_{total}, AP, and rebound AP. With the help of the validated model, we were able to elucidate certain underlying biophysical mechanisms.

3.1.1 Comparison of experimental recordings and simulation outputs of the UAN total membrane current(I_{total})

After multiple iterations of adjusting ion channel conductances in the model to align with experimental data, a closer match was achieved, as depicted in Fig. 4B. Some discrepancies in the two phases of the total membrane current persisted, identified as points a, b, and c in Fig. 4B. Focusing on active ion channels (Kv1.4, Kv4, and Kv1.1), manual tuning was performed to improve the fit with experimental data. The resulting UAN model outputs (solid lines, Fig. 4A) were overlaid on the experimental trace (dotted lines, Fig. 4A) after multiple iterations. The model's peak transient inward current closely matched the experimental trace, with amplitudes of −2.77 nA and −2.76 nA, respectively. Similarly, in the second phase, the model closely approximated the experimental outward current with amplitudes of 1.44 nA and 1.42 nA. At the 15 ms mark, the experimental current was 0.88 nA, while the model output was 0.9 nA. The Root Mean Square Error (RMSE) of 0.16 indicated a good fit between the simulated output and the experimental trace, affirming the model's accuracy. Feature measurements are summarized in Table 4.

3.1.2 Comparison of the experimental recordings and simulation outputs of the UAN AP

In accordance with the experimental protocol, we conducted a current clamp simulation with a delay of 35 mV, a duration of 250 ms, and an amplitude of 4 pA. In the preliminary simulation, the action potential (AP) corresponding to the total membrane current Fig. 4B was examined (Supplementary Fig. S1). Here, we observed a notable disparity in the amplitude of the AP and the hyperpolarization
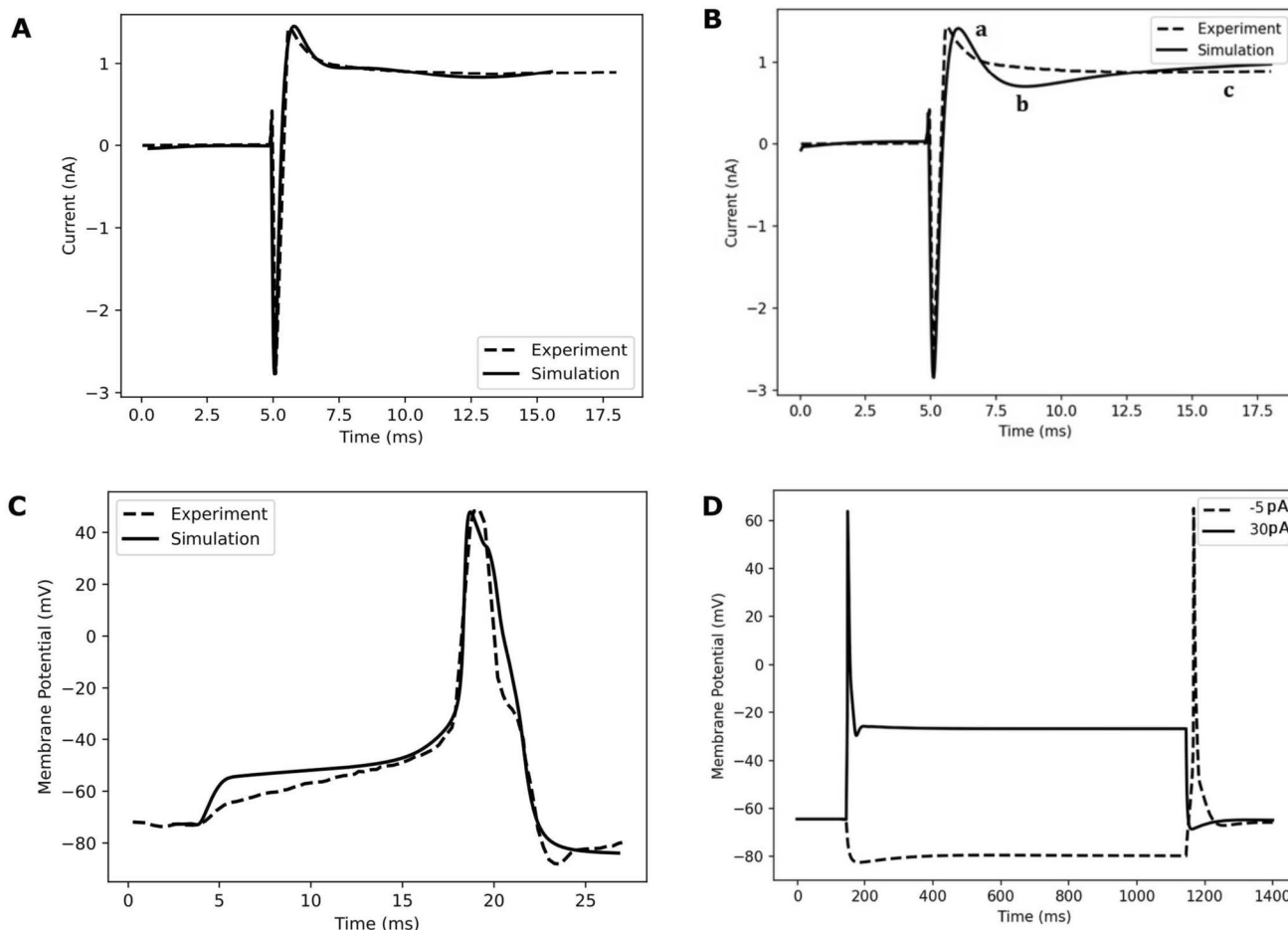
Fig. 4 **A**: The total current of the UAN generated by the model (continuous line) is superimposed with experimental trace (dotted lines). Note that the three phases of the membrane current in the experimental data discussed in Fig. 2A are observed to be closely matched with the simulated output. **B**: The total current of the UAN generated by the model (continuous line) is superimposed with experimental trace (dotted lines). Three sections marked a, b, and c on the figure still show deviation from the experimental trace. **C**: The action potential generated by the model (continuous line) is superimposed with experimental AP (dotted lines) (Kanda et al., 2016). A current clamp of 4 pA amplitude and 250 ms duration was used. Note that the amplitude and width of the AP in both experimental and simulated output are similar. **D**: The simulation result shown with continuous lines is the membrane potential when a current clamp of 30 pA was given. The dashed lines show hyperpolarisation-induced action potential in response to a hypolarising pulse of 5 pA, a characteristic feature of UAN. The duration was 1000 ms in both cases

phase. Subsequently, after fine-tuning the model, the final simulation yielded an AP that closely matched both the experimental trace (depicted by dashed lines) and the

Table 4 Feature values (see Fig. 3A for details) for the UAN total membrane current in the experimental, DRG model and UAN model simulated curves. The corresponding percentage difference relative to the experimental trace is shown in brackets

Features	Experimental	DRG model value	UAN model value
A1	–2.76 nA	–2.77 (0.3) nA	–2.77 (0.3) nA
A2	1.42 nA	0.87 (48) nA	1.44 (1.3) nA
tf	0.10 ms	0.16 (46.1) ms	0.08 (22.2) ms
tr	0.37 ms	1.32 (112.4) ms	0.38 (2.6) ms
τ	0.84 ms	-	0.85 (1.1) ms
HW1	0.22 ms	0.52 (81) ms	0.22 (0) ms
HW2	0.72 ms	-	0.94 (22) ms

simulated output (represented by continuous lines) Fig. 4C. The resting membrane potential (RMP) obtained from experimental studies was measured at -−73.6 mV, a value consistent with that of our model. Specifically, the amplitude of the experimental AP was recorded at 122.4 mV, while the simulated output measured 121.4 mV, both referenced from the RMP.

In accordance with the experimental protocol, we used the current clamp simulation of delay 35 mV, duration 250 ms, and amplitude of 4 pA. In a preliminary simulation, the AP corresponding to the total membrane current (Fig. 4B) is shown in where the discrepancy in the amplitude of the AP and the hyperpolarisation phase is apparent (see Supplementary S1). The final tuned model exhibited an AP as shown in Fig. 4C, the experimental trace (dashed lines), and the simulated output (continuous line). The resting membrane

potential (RMP) from the experimental studies is -−73.6 mV which was also the same for the model. The amplitude of the experimental AP is 122.4 mV, and the simulated output is at 121.4 mV, measured from RMP.

Validation of the presence of rebound AP in the UAN The UAN displayed hyperpolarisation-activated "sag" potential or "rebound AP" in response to hyperpolarising current injection, while the NUAN did not produce such features. Hence, it is crucial to ascertain whether our model would reproduce this feature in the simulations. The membrane potential output from the simulation results is depicted in Fig. 4D; it shows the response to a current clamp of 30 pA amplitude for a duration of 1000 ms, represented by continuous lines. Additionally, the membrane potential using a hyperpolarization current clamp of 5 pA for 1000 ms, is displayed in Fig. 4D as dashed lines. Notably, the simulation with the hyperpolarization current clamp resulted in the observation of a rebound action potential.

3.2 Statistical validation for UAN model total membrane current and AP

Based on the proposed method of estimation of the RMSE measure, the following are the values obtained for the DRG model and UAN model, compared with the experimentally observed records. Total membrane current curve for the UAN: DRG model, RMSE = 0.35; UAN model, RMSE = 0.16. This clearly indicates that our UAN model is a much better approximation to the experimentally observed values for this neuron.

For the action potential, UAN AP vs DRG model, RMSE = 39.16; UAN AP vs UAN model, RMSE = 7.40. Here again, it can be observed that the UAN models match the experimental data significantly better than the DRG model.

3.3 Feature measurement quantification of total membrane current for UAN

In order to show the closeness of our UAN model results to that of the experimental trace compared to the DRG model we have identified and measured a selection of indices (see methods). From the values shown in Table 4 we can see that the UAN model values are closer to those of the experimental recordings than the DRG model values. In this section, we present a detailed analysis of the total membrane current in the urothelial afferent neuron (UAN) model, comparing it to experimental recordings. The reported percentage differences highlight particular electrical activity characteristics of the UAN, providing insight into how well our computational model matches the experimental data. These quantifications are

a way to judge how accurately our model reproduces physiological responses. For example, our UAN model closely approximates the experimental data based on the observed percentage differences in total membrane current. This shows that the model accurately represents the fundamental electrical characteristics of UAN, which has wider implications for comprehending neuronal function in the urothelium as a whole and activity at the population level.

3.4 Feature measurement quantification of Action potential for UAN

Similar to the feature measurement done for the total membrane current, we used the feature measurement approach to compare the closeness of our UAN model findings to those of the experimental trace compared to the DRG model. The indices' related figure is provided in the methods section. Table 5 shows that the UAN model values are closer to the experimental values than the DRG model values. This section delves into the feature measurements of the action potential (AP) in the urothelial afferent neuron (UAN), comparing simulation outputs with experimental traces. The percentage differences presented offer a quantitative assessment of how well our model reproduces the key characteristics of UAN firing. These numbers can be interpreted in the context of neuronal function. For example, the observed percentage differences in AP properties signify the degree of agreement between the model's predictions and experimental outcomes. This has implications for understanding the sensitivity and excitability of UAN, which play pivotal roles in sensory signalling within the urothelium. These quantifications also offer insightful information about how the UAN model might advance our knowledge of pathological conditions affecting the bladder and population-level activity.

Table 5 Feature measurement values (Fig. 3A) for the UAN AP in the experimental, DRG model, and UAN model simulated curves. The corresponding percentage difference relative to the experimental trace is shown in brackets

Features	Experimental	DRG model value	UAN model value
Onset time	4 ms	8.8 ms (75)	3.93 ms (1.7)
RMP	−71.5 mV	−53.4 mV (28.9)	−68.5 mV (4.2)
Amplitude	120.3 mV	104.6 mV (13.9)	116.4 mV (3.2)
Foot width	13.97 ms	17.53 ms (22.6)	14.07 ms (0.7)
Foot area	0.28 mV-s	0.56 mV-s (66.6)	0.31 mV-s (10.1)
AP width	2 ms	4.5 ms (76.9)	2.7 ms (29.7)
AHP amplitude	16.6 mV	−3.9 mV (322)	15.3 mV (8.1)

Table 6 Feature measurement values (Fig. 3A) for the NUAN total membrane current in the experimental and NUAN model simulated curves. The corresponding error values relative to the experimental trace are shown in brackets

Features	Experimental	NUAN model value
A1	–2.83 nA	–2.92 (+0.09) nA
A2	2.41 nA	2.47 (+0.06) nA
tf	0.095 ms	0.11 (−0.02) ms
tr	0.47 ms	0.44 (+0.03) ms
τ	1.32 ms	1.01 (+0.31) ms
HW1	0.215 ms	0.26 (+0.05) ms
HW2	1.03 ms	1.30 (+0.27) ms

3.5 Using the UAN model to replicate the results for the NUAN

We adopted the UAN model in order to model the NUAN. We used the morphological parameters of the NUAN from the literature (Kanda et al., 2016), and the biophysical parameters, such as the ion channel conductances of various ion channels, were tuned to fit the NUAN experimental curves. According to the experimental studies, similar simulation protocols as the UAN were used for the NUAN model.

3.5.1 Comparison of the experimental recordings and simulation outputs of the NUAN total membrane current(I_{total})

We compared the simulation results with experimental traces of I_{total}, AP, and rebound AP for the NUAN, similar to the UAN model verification.

The experimental I_{total} trace shown was obtained at a voltage step of 10 mV from a baseline of –60 mV. We have used the same experimental protocol (Kanda et al., 2016) in our simulations as well; a voltage clamp stepped from the conditioning level of –60 mV for 4.88 ms to a testing level of 10 mV. The NUAN model outputs were superimposed upon the corresponding experimental traces (shown in dashed lines Fig. 5A). We employed the feature measurement method, similar to that utilised for the total membrane current, to assess how well our UAN model results matched those of the experimental trace compared to the DRG model. The results of the comparison are tabulated in Table 6. The amplitude of the transient inward current at the beginning of the voltage step is -−2.83 nA in the experimental recording, while in the model output, it is -−2.92 nA (see Table 6. In the 2nd phase of the curve, the amplitude of the recorded outward current is 2.41 nA, and the model output is 2.47 nA. The RMSE value calculated for the experimental and the simulated output from the NUAN model was 0.15. The close agreement between the experimental and simulated output gives us confidence that our model is robust enough for further analysis.

3.5.2 Comparison of the experimental recordings and simulation outputs of the NUAN Action potential (AP)

We used the current-clamp simulation of delay 35 mV, duration 250 ms, and amplitude of 4 pA. We have shown in Fig. 5B the experimental trace (dashed lines) along with the simulated output (continuous line). The RMP from the experimental studies is -−73.6 mV. The RMP measured
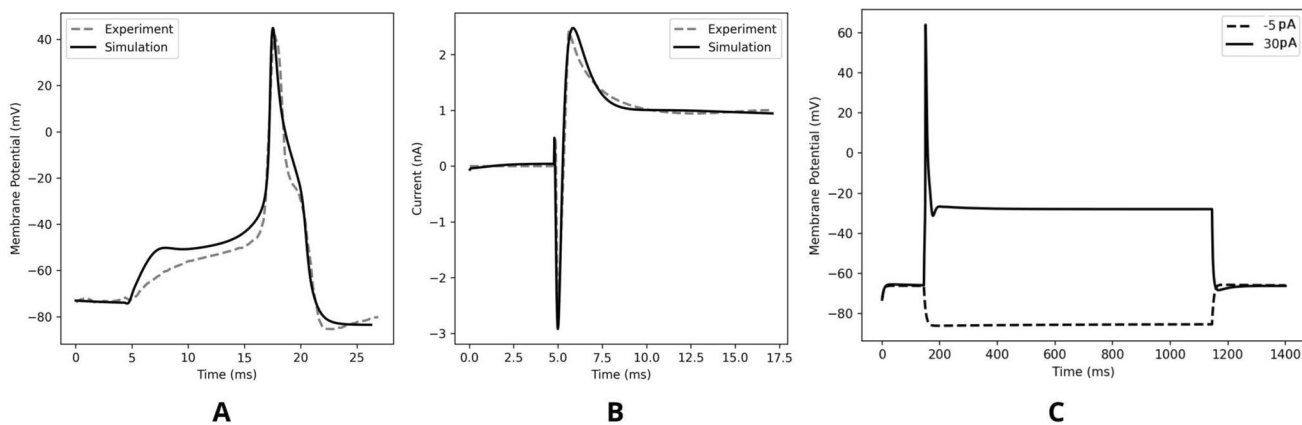

Fig. 5 A: The total current of the NUAN generated by the model (continuous line) is superimposed with experimental trace (dashed lines). **B**: The action potential generated by the model (continuous trace) is superimposed with the experimental AP (dashed lines) (Kanda et al., 2016). A current-clamp of 4 pA amplitude and 250 ms duration was used in both cases. **C**: The continuous trace showed the membrane potential when a current clamp of 30 pA was given and the dashed response to a hyperpolarising pulse of 5 pA. The duration was 1000 ms in both cases

Fig. 6 Sensitivity analysis for K$^+$ channel in UAN AP features on reducing 50% of the conductance of K$^+$ channels present. Kv1.4 channel shows the maximum sensitivity amongst the Kv channels
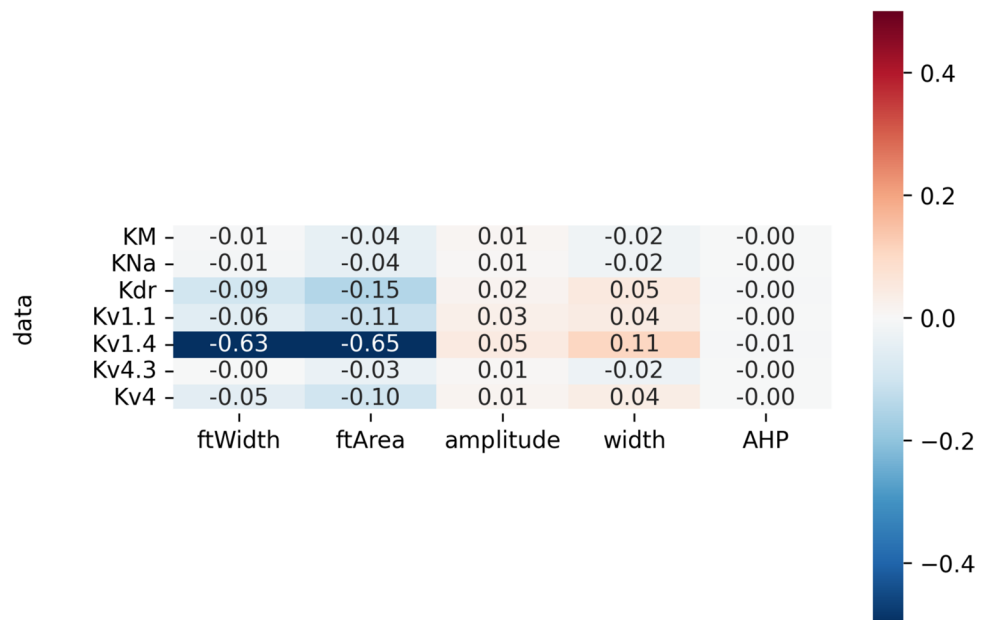
from the model in the absence of the stimulation was also observed to be -−73.6. While the amplitude measured from the RMP of the experimental AP is 122.4 mV, that of the simulated output is 121.4 mV.

Validation of the presence of rebound AP in the NUAN In the experimental studies, NUAN neurons did not exhibit hyperpolarisation-induced AP (rebound AP). The membrane potential output from the simulation from a current clamp of 30 pA amplitude for a duration of 1000 ms is shown as continuous lines in Fig. 5C, and the membrane potential from the simulation result using a current clamp of 5 pA for a duration of 1000 ms (shown as the dashed line in Fig. 5C) did not elicit a rebound action potential, which was in line with the experimental findings.

3.6 Reproducing the experimental response to depolarising pulses and voltage clamp in UAN and NUAN

Our UAN model reproduced the total membrane current trace obtained from the experiment. The experimental investigators hypothesised that Kv4.3/Kv1.4 might be responsible for the differences observed in the A-type current in UAN and NUAN (Kanda et al., 2016). We have shown using our model that the Kv1.4 channel is responsible for the difference. We did a sensitivity analysis for UAN AP Fig. 6, mapping K$^+$ channels present by reducing each of the conductances to 50% and measuring the difference in feature measurement values. Our simulation-based findings were supported by the sensitivity analysis showing that the major K$^+$ channel in phase 2 is the Kv1.4. The presence of rebound action potential in UAN and the absence of one in

NUAN were critical distinguishing features that our model could reproduce. In the experimental studies, UAN exhibited hyperpolarisation-induced action potential (Rebound AP) but not NUAN neurons indicating higher excitability of the urothelial neurons. A possible explanation of this difference in behaviour is the large T-type Ca^{2+} and HCN channel densities in the UAN model. This was tested by reducing the conductance of T-type Ca^{2+} and HCN channel in our NUAN model; we observed that the rebound AP was indeed absent. This is an interesting revelation that could be one of the biophysical reasons behind the increased sensitivity of the UAN compared to the NUAN. Due to the limited availability of experimental data on the UAN, we have used recordings from a single study (Kanda et al., 2016). Further robustness of the UAN model can be tested as and when future experimental studies are undertaken. Our UAN model, besides being used for hypothesis testing and implementing NUAN neurons, is used for modelling urothelial afferent neuron signalling, which is currently in progress.

4 Discussion

We constructed a detailed ionic conductance-based model of the bladder UAN. Though there is ample evidence on the importance of urothelium in the functioning of the bladder, much of it is still unclear. Our UAN model would be the first step towards building a more elaborate model of afferent signalling in the urothelium to help understand urothelial function. The model includes voltage-gated sodium and potassium channels, N, L, P/Q, R, T type Ca^{2+} channels, Calcium-activated K$^+$ channels (BK, SK), HCN channel, TRPV1, TRPM8 channels, and internal calcium dynamics.

Table 7 Predictions and supporting evidence

Prediction	Supporting Evidence	Neuron Type
Type of Kv channel present in UAN neuron	Kv1.4 and Kv4 channels are dominant, with limited Kv4.3 presence.	UAN
Potential contributors to rebound AP in UAN	T-type Ca^{2+} and HCN channels play a significant role.	UAN
Influence of Kv1, Kv4, and Kdr-type channels	Kv1, Kv4, and Kdr-type channels contribute to phase 2 of AP.	UAN
Impact of ion channel conductances on I_{total}	Kv1.4 and Kv4 channels significantly influence transient currents.	UAN
Presence of rebound AP in UAN and NUAN	UAN exhibits rebound AP following hyperpolarization; NUAN does not.	UAN/NUAN

The model reproduced the responses of voltage clamp (see Fig. 4A), depolarising current pulse (See Fig. 4C), and rebound AP (see Fig. 4D). Our model predicts the type of voltage-gated K^+ present in the UAN, namely Kv1.4, Kv1.1, and Kv4. We have also used the UAN model for modelling NUAN and predicted the relative expression of the K^+ and other ion channels in UAN and NUAN. We have also used the model to replicate the presence and absence of rebound AP in UAN and NUAN, respectively.

4.1 Comparison of UAN with small DRG neuron model

Since recent studies have shown differences in the neurons innervating the urothelial and non-urothelial neurons, we set out to model the UAN. Though several preexisting biophysical models are available for different types of neurons, including one on the bladder DRG neuron (Mandge & Manchanda, 2018), we could not adopt it in its reported form for the UAN. The discrepancy is because even after altering the DRG model's morphology to correspond to the UAN and modifying the preexisting ion channel conductances to comply with the experimental data, it was insufficient to achieve a close fit between the experimental and simulated results. Moreover, the calculated RMSE values for AP and I_{total} were found to be 39.16 and 0.35. Hence we concluded that a more customised model at the biophysical level was required for the UAN. The RMSE for UAN AP and I_{total} was calculated as 7.4 and 0.16, respectively. Furthermore, compared to using the DRG model for UAN, the new UAN model is a better physiologically constrained model for the UAN.

In order to select the appropriate ion channels for the UAN, we divided the I_{total} into three phases, the initial transient inward current being caused mainly by Na^+ channels, the second outward current due to inactivating K^+ channels and the last steady outward current due to the non-inactivating K^+ channels. From the simulations on the DRG neuron, we observed that the second phase due to the inactivating K^+ outward current and the third phase due to the non-inactivating K^+ outward current of the simulated curve and the experimental trace did not match. We explored the possibility of other KA and Kdr-type channels to obtain a better fit. Experimental studies show that three types of

A-type Kv channels are present in the DRG, namely Kv1.4, Kv4, and Kv4.3 (Zemel et al., 2018). Of the three types, we wanted to know which of these were present in the UAN neuron. By fine-tuning the maximum conductances of the ion channels using trial and error, we concluded that Kv1.4 and Kv4 were the dominant ones present. We also added a Kdr-type channel, Kv1, which was known to be present in bladder DRG neurons. Hence using the model, we propose an answer to a vital question posed by the experimentalists regarding the type of Kv channel present in the UAN neuron (Kanda et al., 2016).

The reason for the mismatch in the experimental curve and the simulated result from the DRG soma model could be any of the following three. a) It is possible that the DRG soma model was a model of a hypogastric nerve (Fowler et al., 2008). The experiments have not specified the identity of the neuron, and the UAN is from the pelvic nerve. b) The DRG neuron was modeled to fit the results from rat whereas the UAN model is from mouse. c) Experiments were performed on the soma dissociated from the branches for the DRG neuron, whereas for the UAN, they were done on the intact neuron. We have also added the stem, central, and peripheral branches to the soma model as the experimental studies were carried out on the intact neuron. In Table 7 we provide a clear summary of the predictions made based on the distribution of ion channels in the UAN and NUAN neurons. Each prediction is accompanied by a brief description of the supporting evidence or rationale behind it.

4.2 Limitations and avenues for future research

Although we have shown a reasonably strong validation of our UAN model's working, the data used for validating the UAN and NUAN models were procured from a single experimental study. As the studies on UAN and NUAN have only recently been undertaken, we could not obtain other sources for further testing. The robustness of our models could be reinforced when more experimental studies are done on the UAN and NUAN neurons.

There is a discrepancy between the experimental and simulated traces for both UAN and NUAN (shown in Figs. 4C and 5B for UAN and NUAN, respectively) in the initial slow depolarisation phase of the AP; this could be either due to

noise or a missing ion channel or channels in our model. This could be resolved by testing the model against a different set of experimental studies for the UAN and NUAN when such becomes available.

In the future, the following steps might be procedures that may be warranted to augment the robustness of the undertaken work.

Detailed Experimental Characterization: Conduct comprehensive electrophysiological experiments specifically targeting urothelial afferent neurons. This would provide precise data on ion channel properties and kinetics in these neurons.

Comparative Studies: Compare model predictions with additional experimental data beyond the scope of this study. This could include responses to specific pharmacological agents targeting ion channels.

Given that this represents the first such model for UAN/NUAN and considering the limited availability of experimental data, its underconstrained nature is an inherent consequence. This underconstraint is a typical challenge encountered in the preliminary phases of computational neuronal modeling. However, several are published as starting points for further computational and computational with experimental investigation (Medlock et al., 2022). In conclusion, we acknowledge the challenges posed by the underconstrained nature of our model and emphasize the need for further experimental validation and refinement. This work would be a starting point to initiate experimental collaborations to enhance the accuracy and predictive power of our computational model.

4.3 Conclusion

We constructed a detailed biophysical model of the UAN incorporating most, if not all, the conductances that influenced their behavior and validated our model against experimental findings. Our biophysical model has provided valuable insights into the distinct ion channel composition and biophysical properties of UAN and NUAN. Our findings strongly support the hypotheses proposed in this study. Specifically, the presence of Kv1.4 and Kv4 channels in UAN was identified as a critical factor contributing to the differences in A-type currents between UAN and NUAN. Additionally, our model confirmed that the increased density of T-type Ca^{2+} and HCN channels in UAN is responsible for the presence of rebound action potential in UAN, a phenomenon not observed in NUAN. These discoveries offer a deeper understanding of the cellular mechanisms underlying sensory signalling in the urothelium, providing a valuable foundation for future research in the field of bladder function and dysfunction. Our model of the UAN is envisaged to help further the studies of sensory signalling from the urothelium. Multiple recent studies have underscored the importance of chemical signalling from non-neuronal

cells to primary afferent neurons (Baumbauer et al., 2015). Urothelial dysfunction appears to be a pathophysiological component of symptom development in interstitial cystitis, and UAN mechanisms might be vital to understanding some facets of the dysfunctions. Our UAN model would help build the sensory signal transduction pathway model between the urothelial cell and afferent nerve fiber, thereby aiding in analysing urothelial signalling better. A detailed computational model of the UAN and NUAN will complement experimentation in pinpointing possible therapeutic targets at the cellular level.

Declarations

Ethical approval The manuscript does not contain any studies with human participants or animals performed by any of the authors.

Conflict of interest The authors have no competing interests to declare that are relevant to the content of this article.

References

Akemann, W., & Knöpfel, T. (2006). Interaction of kv3 potassium channels and resurgent sodium current influences the rate of spontaneous firing of purkinje neurons. *Journal of Neuroscience, 26*(17), 4602–4612.

Akemann, W., Lundby, A., Mutoh, H., & Knöpfel, T. (2009). Effect of voltage sensitive fluorescent proteins on neuronal excitability. *Biophysical Journal, 96*(10), 3959–3976.

Amir, R., & Devor, M. (2003a). Electrical excitability of the soma of sensory neurons is required for spike invasion of the soma, but not for through-conduction. *Biophysical Journal, 84*(4), 2181–2191.

Amir, R., & Devor, M. (2003b). Extra spike formation in sensory neurons and the disruption of afferent spike patterning. *Biophysical Journal, 84*(4), 2700–2708.

Andersson, K.-E. (2002). Bladder activation: afferent mechanisms. *Urology, 59*(5), 43–50. https://doi.org/10.1016/s0090-4295(01)01637-5

Andersson, K.-E., & Arner, A. (2004). Urinary bladder contraction and relaxation: physiology and pathophysiology. *Physiological Reviews, 84*(3), 935–986.

Apodaca, G., Kiss, S., Ruiz, W., Meyers, S., Zeidel, M., & Birder, L. (2003). Disruption of bladder epithelium barrier function after spinal cord injury. *American Journal of Physiology-Renal Physiology, 284*(5), 966–976. https://doi.org/10.1152/ajprenal.00359.2002

Aruljothi, S., Mandge, D., Manchanda, R. (2017). A biophysical model of heat sensitivity in nociceptive c-fiber neurons. In: *2017 8th International IEEE/EMBS Conference on Neural Engineering (NER)*, pp. 596–599. IEEE

Baker, M. D. (2005). Protein kinase c mediates up-regulation of tetrodotoxin-resistant, persistent na+ current in rat and mouse sensory neurones. *The Journal of Physiology, 567*(3), 851–867.

Baumbauer, K. M., DeBerry, J. J., Adelman, P. C., Miller, R. H., Hachisuka, J., Lee, K. H., Ross, S. E., Koerber, H. R., Davis, B. M., & Albers, K. M. (2015). Keratinocytes can modulate and directly initiate nociceptive responses. *Elife, 4*, 09674.

Birder, L. A., & Groat, W. C. (2007). Mechanisms of disease: involvement of the urothelium in bladder dysfunction. *Nature Clinical Practice Urology, 4*(1), 46–54. https://doi.org/10.1038/ncpuro0672

Bischoff, U., Vogel, W., & Safronov, B. V. (1998). Na+-activated k+ channels in small dorsal root ganglion neurones of rat. *The Journal of Physiology, 510*(3), 743–754.

Black, J. A., Cummins, T. R., Yoshimura, N., Groat, W. C., & Waxman, S. G. (2003). Tetrodotoxin-resistant sodium channels nav1. 8/sns and nav1. 9/nan in afferent neurons innervating urinary bladder in control and spinal cord injured rats. *Brain Research, 963*(1–2), 132–138.

Chambers, J. D., Bornstein, J. C., Gwynne, R. M., Koussoulas, K., & Thomas, E. A. (2014). A detailed, conductance-based computer model of intrinsic sensory neurons of the gastrointestinal tract. *American Journal of Physiology-Gastrointestinal and Liver Physiology, 307*(5), 517–532.

Choi, J.-S., & Waxman, S. G. (2011). Physiological interactions between nav1. 7 and nav1. 8 sodium channels: a computer simulation study. *Journal of Neurophysiology, 106*(6), 3173–3184.

DeBerry, J., Albers, K., & Davis, B. (2013). Bladder hypersensitivity and transcriptional regulation of potassium channel subunit mrna expression in mice with cystitis. *The Journal of Pain, 14*(4), 57.

Du, X., Hao, H., Gigout, S., Huang, D., Yang, Y., Li, L., Wang, C., Sundt, D., Jaffe, D. B., Zhang, H., et al. (2014). Control of somatic membrane potential in nociceptive neurons and its implications for peripheral nociceptive transmission. *PAIN®, 155*(11), 2306–2322.

Fowler, C. J., Griffiths, D., & De Groat, W. C. (2008). The neural control of micturition. *Nature Reviews Neuroscience, 9*(6), 453–466.

Fox, A., Nowycky, M., & Tsien, R. (1987). Single-channel recordings of three types of calcium channels in chick sensory neurones. *The Journal of Physiology, 394*(1), 173–200.

Fukumoto, N., Kitamura, N., Niimi, K., Takahashi, E., Itakura, C., & Shibuya, I. (2012). Ca2+ channel currents in dorsal root ganglion neurons of p/q-type voltage-gated ca2+ channel mutant mouse, rolling mouse nagoya. *Neuroscience Research, 73*(3), 199–206.

Groat, W. C., Yoshimura, N. (2009). Afferent nerve regulation of bladder function in health and disease. *Sensory Nerves*, 91–138.

Groat, W. C., Griffiths, D., & Yoshimura, N. (2015). Neural control of the lower urinary tract. *Comprehensive Physiology, 5*(1), 327.

Han, C., Estacion, M., Huang, J., Vasylyev, D., Zhao, P., Dib-Hajj, S. D., & Waxman, S. G. (2015). Human nav1. 8: enhanced persistent and ramp currents contribute to distinct firing properties of human drg neurons. *Journal of Neurophysiology, 113*(9), 3172–3185.

Hayashi, Y., Takimoto, K., Chancellor, M. B., Erickson, K. A., Erickson, V. L., Kirimoto, T., Nakano, K., Groat, W. C., & Yoshimura, N. (2009). Bladder hyperactivity and increased excitability of bladder afferent neurons associated with reduced expression of kv1. 4 α-subunit in rats with cystitis. *American Journal of Physiology-Regulatory, Integrative and Comparative Physiology, 296*(5), 1661–1670.

Hilaire, C., Diochot, S., Desmadryl, G., Richard, S., & Valmier, J. (1997). Toxin-resistant calcium currents in embryonic mouse sensory neurons. *Neuroscience, 80*(1), 267–276.

Hines, M. L., & Carnevale, N. T. (1997). The neuron simulation environment. *Neural Computation, 9*(6), 1179–1209.

Hodgkin, A. L., & Rushton, W. A. H. (1946). The electrical constants of a crustacean nerve fibre. *Proceedings of the Royal Society B, 133*, 444–479.

Hougaard, C., Fraser, M., Chien, C., Bookout, A., Katofiasc, M., Jensen, B., Rode, F., Bitsch-Nørhave, J., Teuber, L., Thor, K.,

et al. (2009). A positive modulator of kca2 and kca3 channels, 4, 5-dichloro-1, 3-diethyl-1, 3-dihydro-benzoimidazol-2-one (ns4591), inhibits bladder afferent firing in vitro and bladder overactivity *in vivo. Journal of Pharmacology and Experimental Therapeutics, 328*(1), 28–39.

Kanda, H., Clodfelder-Miller, B. J., Gu, J. G., Ness, T. J., & DeBerry, J. J. (2016). Electrophysiological properties of lumbosacral primary afferent neurons innervating urothelial and non-urothelial layers of mouse urinary bladder. *Brain Research, 1648*, 81–89.

Kovalsky, Y., Amir, R., & Devor, M. (2009). Simulation in sensory neurons reveals a key role for delayed na+ current in subthreshold oscillations and ectopic discharge: implications for neuropathic pain. *Journal of Neurophysiology, 102*(3), 1430–1442.

Lei, Q., Pan, X.-Q., Villamor, A. N., Asfaw, T. S., Chang, S., Zderic, S. A., & Malykhina, A. P. (2013). Lack of transient receptor potential vanilloid 1 channel modulates the development of neurogenic bladder dysfunction induced by cross-sensitization in afferent pathways. *Journal of Neuroinflammation, 10*(1), 1–18.

Mandge, D., & Manchanda, R. (2018). A biophysically detailed computational model of bladder small drg neuron soma. *PLoS Computational Biology, 14*(7), 1006293.

Masoli, S., Solinas, S., & D'Angelo, E. (2015). Action potential processing in a detailed purkinje cell model reveals a critical role for axonal compartmentalization. *Frontiers in Cellular Neuroscience, 9*, 47.

Matsuyoshi, H., Masuda, N., Chancellor, M. B., Erickson, V. L., Hirao, Y., Groat, W. C., Wanaka, A., & Yoshimura, N. (2006). Expression of hyperpolarization-activated cyclic nucleotide-gated cation channels in rat dorsal root ganglion neurons innervating urinary bladder. *Brain Research, 1119*(1), 115–123.

Medlock, L., Sekiguchi, K., Hong, S., Dura-Bernal, S., Lytton, W. W., & Prescott, S. A. (2022). Multiscale computer model of the spinal dorsal horn reveals changes in network processing associated with chronic pain. *Journal of Neuroscience, 42*(15), 3133–3149.

Merrill, L., Gonzalez, E. J., Girard, B. M., & Vizzard, M. A. (2016). Receptors, channels, and signalling in the urothelial sensory system in the bladder. *Nature Reviews Urology, 13*(4), 193–204.

Nickel, J. C., Jain, P., Shore, N., Anderson, J., Giesing, D., Lee, H., Kim, G., Daniel, K., White, S., Larrivee-Elkins, C., et al. (2012). Continuous intravesical lidocaine treatment for interstitial cystitis/bladder pain syndrome: safety and efficacy of a new drug delivery device. *Science Translational Medicine, 4*(143), 143–100143100.

Passmore, G. M., Selyanko, A. A., Mistry, M., Al-Qatari, M., Marsh, S. J., Matthews, E. A., Dickenson, A. H., Brown, T. A., Burbidge, S. A., Main, M., et al. (2003). Kcnq/m currents in sensory neurons: significance for pain therapy. *Journal of Neuroscience, 23*(18), 7227–7236.

Rastogi, P., Rickard, A., Dorokhov, N., Klumpp, D. J., & McHowat, J. (2008). Loss of prostaglandin e2release from immortalized urothelial cells obtained from interstitial cystitis patient bladders. *American Journal of Physiology-Renal Physiology, 294*(5), 1129–1135. https://doi.org/10.1152/ajprenal.00572.2007

Ritter, A. M., Martin, W. J., & Thorneloe, K. S. (2009). The voltage-gated sodium channel nav1. 9 is required for inflammation-based urinary bladder dysfunction. *Neuroscience Letters, 452*(1), 28–32.

Rohatgi, A. (2022). Webplotdigitizer: Version 4.6. https://automeris.io/WebPlotDigitizer

Salzer, I., Gantumur, E., Yousuf, A., & Boehm, S. (2016). Control of sensory neuron excitability by serotonin involves 5ht2c receptors and ca2+-activated chloride channels. *Neuropharmacology, 110*, 277–286.

Schmidt-Hieber, C., & Bischofberger, J. (2010). Fast sodium channel gating supports localized and efficient axonal action potential initiation. *Journal of Neuroscience, 30*(30), 10233–10242.

Shieh, C.-C., Turner, S., Zhang, X.-F., Milicic, I., Parihar, A., Jinkerson, T., Wilkins, J., Buckner, S., & Gopalakrishnan, M. (2007). A-272651, a nonpeptidic blocker of large-conductance

ca2+-activated k+ channels, modulates bladder smooth muscle contractility and neuronal action potentials. *British journal of pharmacology, 151*(6), 798–806.

Solinas, S., Forti, L., Cesana, E., Mapelli, J., De Schutter, E., & D'Angelo, E. (2007). Computational reconstruction of pacemaking and intrinsic electroresponsiveness in cerebellar golgi cells. *Frontiers in Cellular Neuroscience, 1*, 2.

Sundt, D., Gamper, N., & Jaffe, D. B. (2015). Spike propagation through the dorsal root ganglia in an unmyelinated sensory neuron: a modeling study. *Journal of Neurophysiology, 114*(6), 3140–3153.

Takahashi, R., Yoshizawa, T., Yunoki, T., Tyagi, P., Naito, S., De Groat, W. C., & Yoshimura, N. (2013). Hyperexcitability of bladder afferent neurons associated with reduction of kv1. 4 α-subunit in rats with spinal cord injury. *The Journal of Urology, 190*(6), 2296–2304.

Tong, W.-C., Choi, C. Y., Karche, S., Holden, A. V., Zhang, H., & Taggart, M. J. (2011). A computational model of the ionic currents, ca 2+ dynamics and action potentials underlying contraction of isolated uterine smooth muscle. *PloS One, 6*(4), 18685.

Usachev, Y. M., & Thayer, S. A. (1999). Ca2+ influx in resting rat sensory neurones that regulates and is regulated by ryanodine-sensitive ca2+ stores. *The Journal of Physiology, 519*(1), 115–130.

Yoshimura, N. (1999). Bladder afferent pathway and spinal cord injury: possible mechanisms inducing hyperreflexia of the urinary bladder. *Progress in Neurobiology, 57*(6), 583–606.

Yoshimura, N., Bennett, N. E., Hayashi, Y., Ogawa, T., Nishizawa, O., Chancellor, M. B., De Groat, W. C., & Seki, S. (2006). Bladder overactivity and hyperexcitability of bladder afferent neurons after intrathecal delivery of nerve growth factor in rats. *Journal of Neuroscience, 26*(42), 10847–10855.

Yoshimura, N., & Chancellor, M. B. (2003). Neurophysiology of lower urinary tract function and dysfunction. *Reviews in Urology, 5*(Suppl 8), 3.

Yoshimura, Y., & Yamaguchi, O. (1997). Calcium independent contraction of bladder smooth muscle. *International Journal of Urology, 4*(1), 62–67. https://doi.org/10.1111/j.1442-2042.1997.tb00142.x

Zemel, B. M., Ritter, D. M., Covarrubias, M., & Muqeem, T. (2018). A-type kv channels in dorsal root ganglion neurons: diversity, function, and dysfunction. *Frontiers in Molecular Neuroscience, 11*, 253.